Semi-Annual Variation of OH* Emission at Mid-Latitudes

Mykhaylo Grygalashvyly[1], Alexander I. Pogoreltsev[2], Alexey B., Andreyev[3], Sergei P. Smyshlyaev[2], and Gerd R. Sonnemann[1]

[1]Leibniz-Institute of Atmospheric Physics at the University Rostock in Kühlungsborn, Schloss-Str.6, D-18225 Ostseebad Kühlungsborn, Germany

[2]Department of Meteorological Forecasting, Russian State Hydrometeorological University (RSHU), Saint-Petersburg, Russia

[3]Institute of the Ionosphere, Almaty, Kazakhstan

Abstract.

The ground-based observations show a phase shift of semi-annual variation of excited hydroxyl (OH*) emissions at mid-latitudes (43° N) compared to those at low latitudes. This differs from the annual cycle at high latitudes. We examine this behavior based on an advanced model of excited hydroxyl production/relaxation, which is part of the 3D chemistry-transport model (CTM). By modelling this, we study the morphology of the excited hydroxyl emission layer at mid-latitudes (30° N -50° N), and we assess the impact of the main drivers on semi-annual variation of excited hydroxyl layer at mid-latitudes: temperature, atomic oxygen, and air density. We found that such a shift of the semi-annual cycle is determined mainly by the superposition of atomic oxygen and annual temperature cycles. The winter peak for emission is determined exclusively by the atomic oxygen concentration, whereas the summer peak is the superposition of all impacts, with temperature taking a leading role.

1. Introduction

Since the second-half of the 20th century, the emissions of excited hydroxyl have been used for three main directions: 1) to infer information about temperature and its long-term

changes; 2) to obtain distributions of minor chemical constituents (ozone, atomic hydrogen, and atomic oxygen) in the mesopause region; and 3) for investigations of dynamic processes such as sudden stratospheric warmings (SSWs), quasi-biennial oscillation (QBO), gravity waves (GWs), planetary waves (PWs), and tides.

Hence, a number of authors have derived temperatures for the mesopause using ground-based observations (Bittner et al., 2000; Holmen et al., 2014). Bittner et al. (2002), Espy and Stegman (2002), Offermann et al. (2010), Holmen et al. (2014), and Dalin et al. (2020) inferred temperature trends in the mesopause region by means of this technique. A large number of investigations have focused on seasonal variations of temperature (e.g. Espy et al., 2007; Reid et al., 2017). The solar-cycle effect on temperature by means of OH* emissions was investigated in works by Espy and Stegman (2002), Pertsev and Perminov (2008), Offermann et al. (2010), Holmen et al. (2014) and Kalicinsky et al. (2016).

Minor chemical constituents as well as chemical heat have also been the focus of airglow observations. Since the first determination of atomic oxygen concentration by the rocket-born detection of OH* airglow (Good, 1976), this method has come into wide use. Russell et al. (2005), Smith et al. (2010) and Mlynczak et al. (2013 a, b) retrieved atomic oxygen density through satellite-based observations of emissions from OH* Meinel bands. Smith et al. (2009) used airglow measurements to derive the ozone concentration, and Thomas (1990), Takahashi et al. (1996), and Mlynczak et al. (2014) retrieved atomic hydrogen, which is almost impossible to infer using other methods at mesopause altitudes. The exothermic chemical heat was derived by airglow measurements in the work by Mlynczak et al. (2013b).

Numerous works, which used airglow observations, have been devoted to dynamic processes. Thus, Shepherd et al. (2010) and Damiani et al. (2010) applied OH* airglow measurements to study mesopause variabilities in time of SSWs. Gao et al. (2011) studied the temporal evolution of nightglow brightness and height during SSW events. A year earlier, they found a QBO signal in the excited hydroxyl emission (Gao et al., 2010). The climatology of PWs was

investigated in works by Takahashi et al. (1999), Buriti et al. (2005), Lopez-Gonzalez et al. (2009), Reisin et al. (2014), and tides were studied in papers by Lopez-Gonzalez et al. (2005) and Xu et al. (2010). GW parameters based on the airglow technique were investigated, for example, in works by Taylor et al. (1991, 1998), Wachter et al. (2015). Shepherd et al. (2012) give a more complete description of works, in which hydroxyl emissions were used to study dynamic processes.

The morphology of the OH* layer is an essential subject for the interpretation of observations and for understanding the processes involved in layer variability. Annual variations of the OH* layer have been identified at all latitudes (Marsh et al., 2006). The semi-annual variations near the equator and at low latitudes have been observed by satellites (Abreu and Yee, 1989; Marsh et al. 2006; Liu et al., 2008) as well as by ground-based instruments (Takahashi et al., 1995), and have been modeled by several research teams (Le Texier et al., 1987; Marsh et al., 2006; Liu et al., 2008). Peak emissions were found to occur near equinoxes. In spite of large number of studies on this subject, there are still gaps in our knowledge. Recently, the unexpected behavior of hydroxyl emissions semi-annual cycle with a shift of the peaks from equinoxes to summer and winter at middle latitudes has been found by ground based observations (Popov et al., 2018; Popov et al., 2020) and independently by modelling (Grygalashvyly et al., 2014, Fig. 3). Similar variations in OH* emissions with peaks near equinoxes have been observed at middle latitudes (34.6° N) in the southern hemisphere (Reid et al., 2014). These results were provided without explanations for them; in our short note, we offer a preliminary explanation.

The manuscript is structured as follows: in the second section, we describe the observational technique and model that were applied; in the third section, we present some results and an analysis of observations and modelling; the concluding remarks and summary are provided in the last section.

2. Observational technique and model

2.1. Observational technique

The spectral airglow temperature imager (SATI), which measures nightglow intensity for vibrational transitions of $OH^{*}_{v=6} \rightarrow OH^{*}_{v=2}$ and temperature using vibrational-rotational transitions, is assembled at the Institute of Ionosphere (43° N, 77° E) in Almaty, Kazakhstan. It represents a Fabry-Perot spectrometer with a CCD (charge-coupled device) camera as a detector and a narrow-band interference filter as the etalon. Following Lopez-Gonzalez et al. (2007), we use an interference filter with the center at 836.813 nm and a bandwidth of 0.182 nm. This corresponds to the spectral region of the OH*(6-2) band. In order to infer the temperature, the calculated spectra for different vibro-rotational transitions are compared with those from observations. The SATI operates at a sixty seconds exposure that provides corresponding time resolution. The method of temperature retrieval is well-described by Lopez-Gonzalez et al. (2004). The observations of temperature were validated using satellite SABER measurements (Lopez-Gonzalez et al., 2007; Pertsev et al., 2013). Additional details about this instrument can be found in a number of works (Wies et al., 1997; Aushev et al., 2000; Lopez-Gonzalez et al., 2004, 2005, 2007, 2009).

2.2. Model and numerical experiment

The model of the excited hydroxyl (MEH) calculates the OH* number densities at each vibrational level *v* as the ratio of production term to the loss term (excited hydroxyl is assumed in the photochemical equilibrium). In the production and loss terms, we summarize contributions due to the chemical reactions, deactivation by quenching and spontaneous emission:

$$[OH_v] = \frac{\begin{pmatrix} f_v k_1[H][O_3] + e_v k_2[HO_2][O] + \sum_{v'=v+1}^{9} p_{v'v}[OH_{v'}][O] + q_{v+1}[OH_{v+1}][N_2] + \\ + \sum_{v'=v+1}^{9} Q_{v'v}[OH_{v'}][O_2] + \sum_{v'=v+1}^{9} A_{v'v}[OH_{v'}] \end{pmatrix}}{\begin{pmatrix} k_3(v)[O] + \sum_{v''=0}^{v-1} p_{vv''}[O] + q_v[N_2] + \\ + \sum_{v''=0}^{v-1} Q_{vv''}[O_2] + \sum_{v''=0}^{v-1} A_{vv''} \end{pmatrix}}, \begin{pmatrix} v < v' \\ v'' < v \end{pmatrix}. \quad (1)$$

The first term in the numerator of (1) is the reaction of ozone with atomic hydrogen, where k_1 is the reaction rate and f_v is the nascent distribution according to Adler-Golden (1997). The second term is the reaction of hydroperoxy with atomic oxygen, where k_2 and e_v are the reaction rate and nascent distribution, respectively (e.g. Takahashi and Batista, 1981; Kaye, 1988). The 3rd, 4th and 5th terms are the transitions from the highest vibrational levels due to quenching, where *p*, *q*, *Q* are the rates for quenching by atomic oxygen (Caridade et al., 2013), molecular nitrogen (Makhlouf et al., 1995) and molecular oxygen (Adler-Golden, 1997), respectively. The last term represents multi-quantum transitions due to spontaneous emissions with Einstein coefficients $A_{v'v}$ following Xu et al. (2012). The loss, additionally, includes the reaction of excited hydroxyl with atomic oxygen, where $k_3(v)$ is the vibrationally dependent reaction rate (Varandas et al., 2004). This model is incorporated into the chemistry-transport model (CTM).

Here, we enumerate only the main features of the CTM, because one can find extended descriptions in a large number of papers (e.g., Sonnemann and Grygalashvyly, 2020; Grygalashvyly et al., 2014; and references therein). The model consists of four blocks: chemical, transport, radiative, and diffusive. The chemical block takes into account 19 constituents, 49 chemical reactions and 14 photodissociation processes. The reaction rates used in the model are taken from Burkholder et al. (2015). The chemistry is based on a family concept (Shimazaki, 1985), considering the odd-hydrogen (H, OH, HO_2, H_2O_2), the odd-oxygen (O, O(^{1}D), O_3), and the odd-nitrogen (NO, NO_2, N(^{4}S), N(^{2}D)) families. In the radiative part, the dissociation rates are taken from a pre-calculated library depending on height and zenith angle (Kremp et al., 1999). The transport block calculates advections in three directions following Walcek (2000). The diffusive part takes into account only vertical

turbulent and molecular diffusivity according to Colegrove et al. (1965), and Morton and Mayers (1994). This model has been validated against observations of ozone, which takes part in OH* formation (e.g. Hartogh et al., 2011; Sonnemann et al., 2007; and references therein), and water vapour, which is the principal source of odd-hydrogens, and particularly of atomic hydrogen (e.g. Hartogh et al., 2010; Sonnemann et al., 2008; and references therein). Our current analysis is based on the calculations for year 2009. This run was published and described in works by Grygalashvyly et al. (2014), section 4, and Sonnemann et al. (2015).

For the model results we assume the equivalence of longitudinal directed structures to local time dependencies over a day, with midnight linked to midnight at Greenwich longitude. The local times of successive longitudes are employed to analyze the data. Hence, in the following figures related to the model results, the longitude is used as the so-called pseudo time. The nighttime averaged values take into account the period from 21:45 LT to 2:15 LT. For the purposes of our discussion, we use the so-called pseudo altitude $z^* = -H \ln(p/p_0)$, where p is pressure, $p_0 = 1013\ mbar$ is the surface pressure, and $H = 7\ km$ is the scale height.

3. Results and discussion

Figure 1 a) shows the monthly mean nightly averaged values of the observed annual variability of intensity at 43° N (red line) and modeled annual variability of volume emission at peak of OH* layer at 43.75° N (black line), both for transition $OH^*_{v=6} \rightarrow OH^*_{v=2}$. The error bar shows standard deviation. By the observations as well as by modelling, we can see clear semi-annual variations of emissions with peaks in winter and summer.

A number of works (e.g. Grygalashvyly et al., 2014; Sonnemann et al., 2015; Grygalashvyly, 2015) have shown that the concentration of excited hydroxyl (hence, volume emission and intensity) at peak is directly proportional to the product of the surrounding pressure (hence, it depends on altitude) with atomic oxygen concentration and inversely proportional to the

power of temperature (Eq. A2 in the Appendix). Thus, in order to infer the reasons for this semi-annual variation, one should consider three drivers of OH* variability, namely, temperature, atomic oxygen concentration and height of the layer.

Figure 1 b) shows the monthly mean nightly averaged values of the observed annual variability of temperature at 43° N (red line) and the modelled annual variability of temperature at the peak of the OH* layer at 43.75° N (black line). The observations, as well as the modelling, show minima in summer and maxima in winter. Hence, the temperature decline can be one of the reasons for the summer peak of intensity (and volume emission).

Figures 1 c) and d) depict modelled monthly mean nightly averaged values of atomic oxygen at a peak of $OH^*_{v=6}$ and height of excited hydroxyl peak, respectively, at 43.75° N. The modelling shows the peaks of atomic oxygen concentration in July and December–January, with the largest values in winter. The variation of height through the year occurs between ~90 km and 94 km. This is essential variability and gives input into the variability of the concentration of the surrounding air.

In order to study the morphology of this semi-annual variation and assess the impacts of temperature, atomic oxygen concentration, and height (concentration of air) variability, we calculate one-month sliding averaged values based on the model results. Figure 2 illustrates the modelled annual variability at the peak of $OH^*_{v=6}$ layer: a) volume emission ($OH^*_{v=6} \rightarrow OH^*_{v=2}$), b) temperature, c) atomic oxygen concentration, and d) height.

The summer maximum of volume emission (Fig. 2a) has the strongest values in July and is extended from ~30° N to ~50° N. The summer maximum is stronger than that in winter. The winter maximum has its strongest values in January and a positive gradient into the winter pole direction. At latitudes 30°–50° N, it represents the rest of the annual variation at high latitudes, which occurs because of the annual variability of the general mean circulation and corresponding atomic oxygen fluxes (Marsh et al., 2006; Liu et al., 2008). Similar behavior of the emissions for transition $OH^*_{v=8} \rightarrow OH^*_{v=3}$ was captured by WINDII (Wind Imaging

Interferometer) and modelled by TIME-GCM (Thermosphere-Ionosphere-Mesosphere Electrodynamics General Circulation Model) at 84–88 km (Fig. 5 and 6; Liu et al., 2008).

The temperature (Fig. 2b) shows a clear annual variation from the middle to the high latitudes, with a minimum ~150 K at middle latitudes in July. The summer minimum at the middle latitudes is the echo of those at high latitudes. The atomic oxygen (Fig. 2c) reveals annual cycle with larger concentrations in winter and smaller concentrations in summer (Smith et al., 2010) at high and middle latitudes beside the region between ~30°–50° N in summer, where it shows one additional peak in June–July. Formation of this summer peak can be explained by the transformed Eulerian mean (TEM) circulation (Limpasuvan et al., 2012, Fig. 7; Limpasuvan et al., 2016, Fig. 5), which brings into the summer hemisphere the air reached by atomic oxygen from the region of its production at high latitudes above 100 km to ~90 km at middle latitudes. The altitude of the peak of the OH* layer (Fig. 2d) shows complex annual variability. There is a secondary maximum OH* peak at ~30°–50° N in summer.

In order to assess input into annual variability from different sources we calculate relative to annual averaged variations of volume emissions due to atomic oxygen, temperature, and air number density (Eq. A6). The derivation of these parameters is presented in the appendix. The similar approach can be useful for an analysis of emission variations due to GWs, PWs, and tides.

Figure 3a shows relative variations of emissions due to impacts of atomic oxygen (black line), temperature (red line), and air density (green line) at 43.75° N. The strongest emission variation occurs because of changes in atomic oxygen concentration. The amplitude of its relative deviation amounts to ~50 %. The amplitudes of relative deviations of emissions due to temperature and air density amount to ~15 % and ~20 %, respectively. The atomic oxygen variation gives the most essential input into the winter maximum of emission (black line). Because of the downward transport of atomic oxygen in winter, the volume emission rises by

~50 % over the annually averaged volume emission. The summer maximum is determined by the superposition of all three factors. After the spring reduction of emissions due to the decline of atomic oxygen concentration (~-40 % of annual averaged values), it rises again up to the approximately annual averaged values in June–July. This is synchronized with the growth of volume emissions by ~20 % over the annual average values due to summer temperature declines (red line) and with the growth of volume emissions by ~15 % over the annual average due to the decline of peak altitude in April–September and the corresponding rise of air density (green line).

Figure 3b illustrates relative variations of emissions due to second momenta (Eq. A7 in the appendix). The second momenta does not give an essential input in annual variation. The strongest among them, $\frac{[O]'M'}{\overline{[O]}\overline{M}}$ (blue line), gives emission variability with an amplitude ~6 % of annual averaged values.

In the context of our short note, the ultimate question about the role of tides and GWs on semi-annual variations of OH* emissions at middle latitudes has not been answered. Undoubtedly, the simultaneous analysis of observations of excited hydroxyl emissions from several stations is desirable to highlight this question.

4. Summary and conclusions

Based on observations and numerical simulation, we confirmed the existence of a semi-annual cycle of OH* emission at middle latitudes. The emission has maxima in summer (June–July) and in winter (December–January). The annual variability of the general mean circulation and corresponding variability of atomic oxygen concentration was found to be the main reason for the winter maximum of the OH* emission. The summer maximum is the superposition of three different processes, namely: atomic oxygen meridional transport due to

residual circulation from the summer pole to the equator; temperature decline, which represents the rest of the mesopause cooling at high latitudes in summer; and the growth of air concentration at the peak of OH* emission layer because of the layer descent at middle latitudes in April–September.

Appendix.

In order to derive the expressions for the variations of excited hydroxyl due to different impacts, we start from a simplified equation for excited hydroxyl concentration.

Taking into account that the ozone is in the photochemical equilibrium in the vicinity of the $[OH_v]$ layer and above at nighttime conditions (Belikovich et al., 2018; Kulikov et al., 2018; Kulikov et al., 2019); utilizing the equation for ozone balance for nighttime ($k_4[O][O_2][M] = k_1[O_3][H] + k_5[O][O_3]$), where k_4 and k_5 are the reaction rates for the reactions of atomic oxygen with molecular oxygen and atomic oxygen with ozone, respectively; omitting the reaction of atomic oxygen with ozone as relatively slow (Smith et al., 2008); substituting the reduced ozone balance equation for the excited hydroxyl balance equation (first term in the numerator of Eq. (1)); assuming that the most effective production of excited hydroxyl occurs due to the reaction of atomic hydrogen with ozone, and the most effective losses are the quenching with molecular oxygen, we obtain from Eq. (1) a simplified expression where excited hydroxyl concentration is represented in terms of atomic oxygen concentration, temperature (in k_4), and concentration of the surrounding air:

$$[OH_v] \approx \mu_v k_4 [O][M]. \qquad (A1)$$

Here $\mu_v = \frac{f_v + \sum_{v'=v+1}^{v'=9} \mu_{v'} Q_{v'v}}{\sum_{v''=0}^{v''=v-1} Q_{vv''}}$, $(f_{v>9} = 0)$ are the coefficients which represent the arithmetic combination of branching ratios f_v and quenching coefficients $Q_{v'v}$. The more comprehensive derivation of (A1) one can find in number of works (e.g. Grygalashvyly et al., 2014;

Grygalashvyly, 2015; Grygalashvyly and Sonnemann, 2020). Although this is too simplified to be used for precise calculations, it is useful for obtaining information about impacts and assessing the variabilities.

Multiplying (A1) by Einstein-coefficient $A_{vv''}$ for given transition, writing reaction rate explicitly $k_4 = 6 \cdot 10^{-34}(300/T)^{2.4}$ (Burkholder et al., 2015), and collecting all constants in $\chi_{vv''}$, we get an expression for volume emission in terms of atomic oxygen concentration, temperature, and air number density:

$$V \approx \chi_{vv''} T^{-2.4}[O][M], \qquad (A2)$$

where $\chi_{vv''} = \mu_v A_{vv''} \cdot 6 \cdot 10^{-34} \cdot 300^{2.4}$.

Next, we apply to the temperature, atomic oxygen concentration, and concentration of air in (A2) Reynolds decomposition by averaged and variable part:

$$V \approx \chi_{vv''}(\bar{T} + T')^{-2.4}\left(\overline{[O]} + [O]'\right)\left(\overline{[M]} + [M]'\right), \qquad (A3)$$

where $\bar{T}$, $\overline{[O]}$, $\overline{[M]}$ are average parts, and $T', [O]', [M]'$ are the corresponding varying parts.

After the decomposing term with temperature in the Taylor expansion and cross-multiplying all terms of (A3), we obtain:

$$V \approx \chi_{vv''}\bar{T}^{-2.4}\overline{[O]} \cdot \overline{[M]} + \chi_{vv''}\bar{T}^{-2.4}\overline{[O]}[M]' + \chi_{vv''}\bar{T}^{-2.4}[O]'\overline{[M]} - 2.4\chi_{vv''}T'\bar{T}^{-3.4}\overline{[O]} \cdot \overline{[M]} + \chi_{vv''}\bar{T}^{-2.4}[O]'[M]' - 2.4\chi_{vv''}T'\bar{T}^{-3.4}\overline{[O]}[M]' - 2.4\chi_{vv''}T'\bar{T}^{-3.4}[O]'\overline{[M]} - 2.4\chi_{vv''}T'\bar{T}^{-3.4}[O]'[M]'. \qquad (A4)$$

The volume emission for a given transition can be represented as follows:

$$V \approx \bar{V} + V'_M + V'_O + V'_T + V''_{OM} + V''_{TM} + V''_{TO} + higher\ momenta, \qquad (A5)$$

where, $\bar{V} = \chi_{vv''}\bar{T}^{-2.4}\overline{[O]} \cdot \overline{[M]}, V'_M = \chi_{vv''}\bar{T}^{-2.4}\overline{[O]}[M]', V'_O = \chi_{vv''}\bar{T}^{-2.4}[O]'\overline{[M]}, V'_T = -2.4\chi_{vv''}T'\bar{T}^{-3.4}\overline{[O]} \cdot \overline{[M]}, V''_{OM} = \chi_{vv''}\bar{T}^{-2.4}[O]'[M]', V''_{TM} = -2.4\chi_{vv''}T'\bar{T}^{-3.4}\overline{[O]}[M]', V''_{TO} = -2.4\chi_{vv''}T'\bar{T}^{-3.4}[O]'\overline{[M]}$.

Hence, relative deviations (RD) of emissions due to variations of atomic oxygen, temperature, and concentration of air are:

$$RD'_O = 100\% \cdot \frac{V'_O}{\bar{V}} = 100\% \cdot \frac{[O]'}{\overline{[O]}},$$
$$RD'_T = 100\% \cdot \frac{V'_T}{\bar{V}} = 100\% \cdot -2.4\frac{T'}{\bar{T}}, \quad (A6)$$
$$RD'_M = 100\% \cdot \frac{V'_M}{\bar{V}} = 100\% \cdot \frac{[M]'}{\overline{[M]}}.$$

The relative deviations (RD) of emission due to second momenta are

$$RD''_{OM} = 100\% \cdot \frac{V''_{OM}}{\bar{V}} = 100\% \cdot \frac{[O]'[M]'}{\overline{[O][M]}},$$
$$RD''_{TM} = 100\% \cdot \frac{V''_{TM}}{\bar{V}} = 100\% \cdot -2.4\frac{T'[M]'}{\bar{T}\overline{[M]}}, \quad (A7)$$
$$RD''_{TO} = 100\% \cdot \frac{V''_{TO}}{\bar{V}} = 100\% \cdot -2.4\frac{T'[O]'}{\bar{T}\overline{[O]}}.$$

Data availability. The data used in this study can be downloaded from http://ra.rshu.ru/files/Grygalashvyly_et_al_ANGEO_2020.

Author contributions. All authors contributed equally to this paper.

Competing interests. The authors declare that they have no conflict of interest.

Acknowledgements. This work was supported by the Russian Science Foundation (grant #20-77-10006). Some data processing have been done under the state task of the Ministry of science and higher education of the Russian Federation (project FSZU-2020-0009)".

References

Abreu, V. J., and Yee, J. H.: Diurnal and seasonal variation of the nighttime OH (8-3) emission at low latitudes, J. Geophys. Res., 94(A9), 11949-11957, doi:10.1029/89JA00619, 1989.

Adler-Golden, S.: Kinetic parameters for OH nightglow modeling consistent with recent laboratory measurements, J. Geophys. Res., 102(A9), 19969–19976, doi:10.1029/97JA01622, 1997.

Aushev, V. M., Pogoreltsev, A. I., Vodyannikov, V. V., Wiens, R. H., and Shepherd, G. G.: Results of the airglow and temperature observations by MORTI at the Almaty site (43.05 N, 76.97 E), Phys. Chem. Earth, 25(5–6), 409–415, doi:10.1016/S1464-1909(00)00035-6, 2000.

Belikovich, M. V., Kulikov, M. Yu., Grygalashvyly, M., Sonnemann, G. R., Ermakova, T. S., Nechaev, A. A., and Feigin, A. M.: Ozone chemical equilibrium in the extended mesopause under the nighttime conditions. Adv. Space Res., 61, 426-432, doi: 10.1016/j.asr.2017.10.010, 2018.

Bittner, M., Offermann, D., and Graef, H. H.: Mesopause temperature variability above a midlatitude station in Europe, J. Geophys. Res., 105(D2), 2045–2058, doi:10.1029/1999JD900307, 2000.

Bittner, M., Offermann, D., Graef, H.-H., Donner, M., and Hamilton, K.: An 18 year time series of OH rotational temperatures and middle atmosphere decadal variations, J. Atmos. Sol. Terr. Phys., 64, 1147-1166, doi:10.1016/S1364-6826(02)00065-2, 2002.

Buriti, R. A., Takahashi, H., Lima, L. M., and Medeiros, A. F.: Equatorial planetary waves in the mesosphere observed by airglow periodic oscillations, Adv. Space Res., 35, 2031–2036, doi: 10.1016/j.asr.2005.07.012, 2005.

Burkholder, J. B., Sander, S. P., Abbatt, J., Barker, J. R., Huie, R. E., Kolb, C. E., Kurylo, M. J., Orkin, V. L., Wilmouth, D. M., and Wine, P. H.: Chemical Kinetics and Photochemical Data for Use in Atmospheric Studies, Evaluation No. 18, JPL Publication 15-10, Jet Propulsion Laboratory, Pasadena, http://jpldataeval.jpl.nasa.gov, 2015.

Caridade, P. J. S. B., Horta, J.-Z. J., and Varandas, A. J. C.: Implications of the O + OH reaction in hydroxyl nightglow modeling, Atmos. Chem. Phys., 13, 1-13, doi:10.5194/acp-13-1-2013, 2013.

Colegrove, F. D., Hanson, W. B., and Johnson, F. S.: Eddy diffusion and oxygen transport in the lower thermosphere, J. Geophys. Res., 70, 4931, doi:10.1029/JZ070i019p04931, 1965.

Dalin, P., Perminov, V., Pertsev, N., and Romejko, V.: Updated long-term trends in mesopause temperature, airglow emissions, and noctilucent clouds, J. Geophys. Res. Atmos., 125, e2019JD030814, doi.org/10.1029/2019JD030814, 2020.

Damiani, A., Storini, M., Santee, M. L., and Wang, S.: Variability of the nighttime OH layer and mesospheric ozone at high latitudes during northern winter: influence of meteorology, Atmos. Chem. Phys., 10, 10291-10303, doi:10.5194/acp-10-10291-2010, 2010.

Espy, P. J., and Stegman, J.: Trends and variability of mesospheric temperature at high-latitudes, Phys. Chem. Earth, 27, 543–553, doi:10.1016/S1474-7065(02)00036-0, 2002.

Espy, P. J., Stegman, J., Forkman, P., and Murtagh, D. P.: Seasonal variation in the correlation of airglow temperature and emission rate, Geophys. Res. Lett., 34, L17802, doi:10.1029/2007GL031034, 2007.

Gao, H., Xu, J., and Wu, Q.: Seasonal and QBO variations in the OH nightglow emission observed by TIMED/SABER, J. Geophys. Res., 115, A06313, doi:10.1029/2009JA014641, 2010.

Gao, H., Xu, J., Ward, W., and Smith, A. K.: Temporal evolution of nightglow emission responses to SSW events observed by TIMED/SABER, J. Geophys. Res., 116, D19110, doi:10.1029/2011JD015936, 2011.

Garcia, R. R., and Solomon, S.: The effect of breaking gravity waves on the dynamics and chemical composition of the mesosphere and lower thermosphere, J. Geophys. Res., 90(D2), 3850–3868, doi:10.1029/JD090iD02p03850, 1985.

Good, R. E.: Determination of atomic oxygen density from rocket borne measurements of hydroxyl airglow, Planet. Space Sci., 24, 389–395, doi:10.1016/0032-0633(76)90052-0, 1976.

Grygalashvyly, M., Sonnemann, G. R., Lübken, F.-J., Hartogh, P., and Berger, U.: Hydroxyl layer: Mean state and trends at midlatitudes, J. Geophys. Res., 119, 12391–12419, doi:10.1002/2014JD022094, 2014.

Grygalashvyly, M.: Several notes on the OH*-layer, Ann. Geophys., 33, 923-930, doi:10.5194/angeo-33-923-2015, 2015.

Grygalashvyly, M., and Sonnemann, G. R.: Note on Consistency between Kalogerakis-Sharma Mechanism (KSM) and Two-Step Mechanism of Atmospheric Band Emission, Earth Planets Space, accepted, 2020.

Hartogh, P., Sonnemann, G. R., Grygalashvyly, M., Li, S., Berger, U., and Lübken, F.-J.: Water vapor measurements at ALOMAR over a solar cycle compared with model calculations by LIMA, J. Geophys. Res., 114, doi:10.1029/2009JD012364, 2010.

Hartogh, P., Jarchow, C., Sonnemann, G. R., and Grygalashvyly, M.: Ozone distribution in the middle latitude mesosphere as derived from microwave measurements at Lindau (51.66° N, 10.13° E), J. Geophys. Res., 116, D04305, doi:10.1029/2010JD014393, 2011.

Holmen, S. E., Dyrland, M. E., and Sigernes, F.: Long-term trends and the effect of solar cycle variations on mesospheric winter temperatures over Longyearbyen, Svalbard (78°N), J. Geophys. Res. Atmos., 119, 6596–6608, doi:10.1002/2013JD021195, 2014.

Kalicinsky, C., Knieling, P., Koppmann, R., Offermann, D., Steinbrecht, W., and Wintel, J.: Long-term dynamics of OH* temperatures over central Europe: trends and solar correlations, Atmos. Chem. Phys., 16, 15033-15047, doi:10.5194/acp-16-15033-2016, 2016.

Kaye, J. A.: On the possible role of the reaction $O + HO_2 \rightarrow OH + O_2$ in OH airglow, J. Geophys. Res., 93, 285–288, doi:10.1029/JA093iA01p00285, 1988.

Kremp, Ch., Berger, U., Hoffmann, P., Keuer, D., and Sonnemann, G. R.: Seasonal variation of middle latitude wind fields of the mesopause region -a comparison between observation and model calculation, Geophys. Res. Lett., 26, 1279-1282, doi:10.1029/1999GL900218, 1999.

Kulikov, M. Yu., Belikovich, M. V., Grygalashvyly, M., Sonnemann, G. R., Ermakova, T. S., Nechaev, A. A., and Feigin, A. M.: Nighttime ozone chemical equilibrium in the mesopause region, J. Geophys. Res., 123, 3228-3242, doi: 10.1002/2017JD026717, 2018.

Kulikov, M. Yu., Nechaev, A. A. , Belikovich, M. V., Vorobeva, E. V., Grygalashvyly, M., Sonnemann, G. R., and Feigin, A. M.: Boundary of Nighttime Ozone Chemical Equilibrium in the Mesopause Region from SABER Data: Implications for Derivation of Atomic Oxygen and Atomic Hydrogen, Gepohys. Res. Lett., 46, 997-1004, doi:10.1029/2018GL080364, 2019.

Le Texier, H., Solomon, S., and Garcia, R. R.: Seasonal variability of the OH Meinel bands, Planet. Space Sci., 35(8), 977-989, doi:10.1016/0032-0633(87)90002-X, 1987.

Limpasuvan, V., Richter, J. H., Orsolini, Y. J., Stordal, F., and Kvissel, O.-K.: The roles of planetary and gravity waves during a major stratospheric sudden warming as characterized by WACCM, J. Atmos. Sol. Terr. Phys., 78–79, 84–98, doi:10.1016/j.jastp.2011.03.004, 2012.

Limpasuvan, V., Orsolini, Y. J., Chandran, A., Garcia, R. R., and Smith, A. K.: On the composite response of the MLT to major sudden stratospheric warming events with elevated stratopause, J. Geophys. Res. Atmos., 121, 4518–4537, doi:10.1002/2015JD024401, 2016.

Liu, G., and Shepherd, G. G.: An empirical model for the altitude of the OH nightglow emission, Geophys. Res. Lett., 33, L09805, doi:10.1029/2005GL025297, 2006.

Liu, G., Shepherd, G. G., and Roble, R. G.: Seasonal variations of the nighttime O(^{1}S) and OH airglow emission rates at mid-to-high latitudes in the context of the large-scale circulation, J. Geophys. Res., 113, A06302, doi:10.1029/2007JA012854, 2008.

Lopez-Gonzalez, M. J., Rodriguez, E., Wiens, R. H., Shepherd, G. G., Sargoytchev, S., Brown, S., Shepherd, M. G., Aushev, V. M., Lopez-Moreno, J. J., Rodrigo, R., and Cho, Y.-M.: Seasonal variations of O_2 atmospheric and OH(6–2) airglow and temperature at mid-latitudes from SATI observations, Ann. Geophys., 22, 819–828, doi: 10.5194/angeo-22-819-2004, 2004.

Lopez-Gonzalez, M. J., Rodriguez, E., Shepherd, G. G., Sargoytchev, S., Shepherd, M. G., Aushev, V. M., Brown, S., Garcia-Comas, M., and Wiens, R. H.: Tidal variations of O_2 Atmospheric and OH(6-2) airglow and temperature at mid-latitudes from SATI observations, Ann. Geophys., 23, 3579–3590, doi:10.5194/angeo-23-3579-2005, 2005.

Lopez-Gonzalez, M. J., Garcia-Comas, M., Rodriguez, E., Lopez-Puertas, M., Shepherd, M. G., Shepherd, G. G., Sargoytchev, S., Aushev, V. M., Smith, S. M., Mlynczak, M. G., Russell, J. M., Brown, S., Cho, Y.-M., and Wiens, R. H.: Ground-based mesospheric temperatures at mid-latitude derived from O_2 and OH (6-2) airglow SATI data: Comparison with SABER measurements, J. Atmos. Solar-Terr. Phys., 69, 2379–2390. doi:10.1016/j.jastp.2007.07.004, 2007.

Lopez-Gonzalez, M. J., Rodríguez, E., Garcia-Comas, M., Costa, V., Shepherd, M. G., Shepherd, G. G., Aushev, V. M., and Sargoytchev, S.: Climatology of planetary wave type oscillations with periods of 2–20 days derived from O_2 atmospheric and OH(6-2) airglow

observations at mid-latitude with SATI, Ann.Geophys., 27, 3645–3662, doi:10.5194/angeo-27-3645-2009, 2009.

Makhlouf, U. B., Picard, R. H., and Winick, J. R.: Photochemical-dynamical modeling of the measured response of airglow to gravity waves. 1. Basic model for OH airglow, J. Geophys. Res., 100, 11289–11311, doi:10.1029/94JD03327, 1995.

Marsh, D. R., Smith, A. K., Mlynczak, M. G., and Russell III, J. M.: SABER observations of the OH Meinel airglow variability near the mesopause, J. Geophys. Res., 111, A10S05, doi:10.1029/2005JA011451, 2006.

Mlynczak, M. G., Hunt, L. A., Mast, J. C., Marshall, B. T., Russell III, J. M., Smith, A. K., Siskind, D. E., Yee, J.-H., Mertens, C. J., Martin-Torres, F. J., Thompson, R. E., Drob, D. P., and Gordley, L. L.: Atomic oxygen in the mesosphere and lower thermosphere derived from SABER: Algorithm theoretical basis and measurement uncertainty, J. Geophys. Res. Atmos., 118, 5724–5735, doi:10.1002/jgrd.50401, 2013a.

Mlynczak, M. G., Hunt, L. A., Mertens, C. J., Marshall, B. T., Russell III, J. M., Lopez-Puertas, M., Smith, A. K., Siskind, D. E., Mast, J. C., Thompson, R. E., and Gordley, L. L.: Radiative and energetic constraints on the global annual mean atomic oxygen concentration in the mesopause region, J. Geophys. Res. Atmos., 118, 5796–5802, doi:10.1002/jgrd.50400, 2013b.

Mlynczak, M. G., Hunt, L. A., Marshall, B. T., Mertens, C. J., Marsh, D. R., Smith, A. K., Russell, J. M., Siskind, D. E., and Gordley, L. L.: Atomic hydrogen in the mesopause region

derived from SABER: Algorithm theoretical basis, measurement uncertainty, and results, J. Geophys. Res., 119, 3516–3526, doi:10.1002/2013JD021263, 2014.

Morton, K. W., and D. F. Mayers, D. F.: Numerical Solution of Partial Differential Equations, Cambridge University Press, 1994.

Offermann, D., Hoffmann, P., Knieling, P., Koppmann, R., Oberheide, J., and Steinbrecht, W.: Long-term Trends and Solar Cycle Variations of Mesospheric Temperature and Dynamics, J. Geophys. Res., 115, D18127, doi:10.1029/2009JD013363, 2010.

Pertsev, N., and Perminov, V.: Response of the mesopause airglow to solar activity inferred from measurements at Zvenigorod, Russia, Ann. Geophys., 26, 1049-1056, doi:10.5194/angeo-26-1049-2008, 2008.

Pertsev N. N., Andreyev A. B., Merzlyakov E. G., and Perminov V. I.: Mesosphere-thermosphere manifestations of strato-spheric warmings: joint use of satellite and ground-based measurements, Current Problems in Remote Sensing of the Earth from Space, 10(1), 93–100, http://jr.rse.cosmos.ru/article.aspx?id=1154&lang=eng, 2013.

Popov, A. A., Gavrilov, N. M., Andreev, A. B., and Pogoreltsev, A. I.: Interannual dynamics in intensity of mesoscale hydroxyl nightglow variations over Almaty, Solar-Terr. Phys., 4(2), 63–68, doi:/10.12737/stp-42201810, 2018.

Popov, A. A., Gavrilov, N. M., Perminov, V. I., Pertsev, N. N., and Medvedeva, I. V.: Multi-year observations of mesoscale variances of hydroxyl nightglow near the mesopause at Tory

and Zvenigorod, J. Atmos. Solar-Terr. Phys., 205, 1-8, doi:10.1016/j.jastp.2020.105311, 2020.

Reid, I. M., Spargo, A. J., and Woithe, J. M.: Seasonal variations of the nighttime O(^{1}S) and OH (8-3) airglow intensity at Adelaide, Australia, J. Geophys. Res. Atmos., 119, 6991–7013, doi:10.1002/2013JD020906, 2014.

Reid, I. M., Spargo, A. J., Woithe, J. M., Klekociuk, A. R., Younger, J. P., and G. G. Sivjee, G. G.: Seasonal MLT-region nightglow intensities, temperatures, and emission heights at a Southern Hemisphere midlatitude site, Ann. Geophys., 35, 567-582, doi:10.5194/angeo-35-567-2017, 2017.

Reisin, E., Scheer, J., Dyrland, M. E., Sigernes, F., Deehr, C. S., Schmidt, C., Höppner, K., Bittner, M., Ammosov, P. P., Gavrilyeva, G. A., Stegman, J., Perminov, V. I., Semenov, A. I., Knlieling, P., Koomann, R., Shiokawa, K., Lowe, R. P., Lopez-Gonzalez, M. J., Rodriguez, E., Zhao, Y., Taylor, M. J., Buriti, R. A., Espy, P. E., French, W. J., Eichmann, K.-U., Burrows, J. P., and von Savigny, C.: Traveling planetary wave activity from mesopause region airglow temperatures determined by the Network for the Detection of Mesospheric Change (NDMC), J. Atmos. Sol.-Terr. Phys., 119, 71–82, doi:10.1016/j.jastp.2014.07.002, 2014.

Russell, J. P., Ward, W. E., Lowe, R. P., Roble, R. G., Shepherd, G. G., and B. Solheim, B.: Atomic oxygen profiles (80 to 115 km) derived from Wind Imaging Interferometer/Upper Atmospheric Research Satellite measurements of the hydroxyl and greenline airglow: Local time–latitude dependence, J. Geophys. Res., 110, D15305, doi:10.1029/2004JD005570, 2005.

Shepherd, G. G., Thuillier, G., Cho, Y.-M., Duboin, M.-L., Evans, W. F. J., Gault, W. A., Hersom, C., Kendall, D. J. W., Lathuillère, C., Lowe, R. P., McDade, I. C., Rochon, Y. J., Shepherd, M. G., Solheim, B. H., Wang, D.-Y., and Ward, W. E.: The Wind Imaging Interferometer (WINDII) on the Upper Atmosphere Research Satellite: A 20 year perspective, Rev. Geophys., 50, RG2007, doi:10.1029/2012RG000390, 2012.

Shepherd, M. G., Cho, Y.-M., Shepherd, G. G., Ward, W., and Drummond, J. R.: Mesospheric temperature and atomic oxygen response during the January 2009 major stratospheric warming, J. Geophys. Res., 115, A07318, doi:10.1029/2009JA015172, 2010.

Shimazaki, T.: Minor constituents in the middle atmosphere, D. Reidel Publishing Company, Dordrecht, Holland, 1985.

Smith, A. K., Marsh, D. R., Russell III, J. M., Mlynczak, M. G., Martin-Torres, F. J., and Kyrölä, E.: Satellite observations of high nighttime ozone at the equatorial mesopause, J. Geophys. Res., 113, D17312, doi:10.1029/2008JD010066, 2008.

Smith, A. K., Lopez-Puertas, M., Garcia-Comas, M., and Tukiainen, S.: SABER observations of mesospheric ozone during NH late winter 2002-2009, Geophys. Res. Lett., 36, L23804, doi:10.1029/2009GL040942, 2009.

Smith, A. K., Marsh, D. R., Mlynczak, M. G., and Mast, J. C.: Temporal variation of atomic oxygen in the upper mesosphere from SABER, J. Geophys. Res., 115, D18309, doi:10.1029/2009JD013434, 2010.

552 Sonnemann, G. R., Hartogh, P., Jarchow., C., Grygalashvyly, M., and Berger, U.: On the
553 winter anomaly of the night-to-day ratio of ozone in the middle to upper mesosphere in
554 middle to high latitudes, Adv. Space Res., 40, 846-854, doi: 10.1016/j.asr.2007.01.039, 2007.
555
556 Sonnemann, G. R., Hartogh, P., Grygalashvyly, M., Li, S., and Berger, U.: The quasi 5-day
557 signal in the mesospheric water vapor concentration in high latitudes in 2003 - a comparison
558 between observations at ALOMAR and calculations, J. Geophys. Res., 113, D04101, doi:
559 10.1029/2007JD008875, 2008.
560
561 Sonnemann, G. R., Hartogh, P., Berger, U., and Grygalashvyly, M.: Hydroxyl layer: trend of
562 number density and intra-annual variability, Ann. Geophys., 33, 749–767, doi:10.5194/angeo-
563 33-749-2015, 2015.
564
565 Sonnemann G., and Grygalashvyly, M.: The slow-down effect in the nighttime mesospheric
566 chemistry of hydrogen radicals, Adv. Space Res., 65, 2800-2807,
567 doi:10.1016/j.asr.2020.03.025, 2020.
568
569 Takahashi, H., and Batista, P. P.: Simultaneous measurements of OH (9,4), (8,3), (7,2), 6,2),
570 and (5,1) bands in the airglow, J. Geophys. Res., 86, 5632–5642,
571 doi:10.1029/JA086iA07p05632, 1981.
572
573 Takahashi, H., Clemesha, B. R., and Batista, P. P.: Predominant semi-annual oscillation of the
574 upper mesospheric airglow intensities and temperatures in the equatorial region, J. Atmos.
575 Terr. Phys., 57(4), 407-414, doi:10.1016/0021-9169(94)E0006-9, 1995.
576

Takahashi, H., Stella, M. L., Clemesha, B. R., Simonich, D. M., Stegman, J., and Witt, G.: Atomic hydrogen and ozone concentration derived from simultaneous lidar and rocket airglow measurements in the equatorial region, J. Geophys. Res., 101, 4033-4040, doi:10.1029/95JD03035, 1996.

Takahashi, H., Batista, P. P., Buriti, R. A, Gobbi, D., Nakamura, T., Tsuda, T., and Fukao, S.: Response of the airglow OH emission, temperature and mesopause wind to the atmospheric wave propagation over Shigaraki, Japan, Earth Planets Space, 51, 863–875, doi:10.1186/BF03353245, 1999.

Taylor, M. J., Espy, P. J., Baker, D. J., Sica, R. J., Neal, P. C., and Pendleton, Jr. W. R.: Simultaneous intensity, temperature and imaging measurements of short period wave structure in the OH nightglow emission, Planet. Space Sci., 39, 1171–1188, doi: 10.1016/0032-0633(91)90169-B, 1991.

Taylor, M. J., Seo, S. H., Nakamura, T., Tsuda, T., Fukunishi, H., and Takahashi, Y.: Long base-line measurements of short-period mesospheric gravity waves during the SEEK campaign, Geophys. Res. Lett., 25, 1797–1800, doi:10.1029/98GL00847, 1998.

Thomas, R. J.: Atomic hydrogen and atomic oxygen density in the mesopause region: Global and seasonal variations deduced from Solar Mesosphere Explorer near-infrared emissions, J. Geophys. Res., 95, 16457-16476, doi:10.1029/JD095iD10p16457, 1990.

Varandas, A. J. C.: Reactive and non-reactive vibrational quenching in O + OH collisions, Chem. Phys. Lett., 396, 182–190, doi:10.1016/j.cplett.2004.08.023, 2004.

Wachter, P., Schmidt, C., Wüst, S., and Bittner, M.: Spatial gravity wave characteristics obtained from multiple OH(3-1) airglow temperature time series, J. Atmos. Sol. Terr. Phys., 135, 192-201, doi: 10.1016/j.jastp.2015.11.008, 2015.

Walcek, C. J.: Minor flux adjustment near mixing ratio extremes for simplified yet highly accurate monotonic calculation of tracer advection, J. Geophys. Res., 105, 9335-9348, doi:10.1029/1999JD901142, 2000.

Wiens, R. H., Moise, A., Brown, S., Sargoytchev, S., Peterson, R. N., Shepherd, G. G., Lopez-Gonzalez, M. J., Lopez-Moreno J. J., and Rodrigo R.: SATI: A spectral airglow tempera-ture imager, Adv. Space Res. 1997, 19, 677–680, doi:10.1016/S0273-1177(97)00162-2, 1997.

Xu, J., Smith, A. K., Jiang, G., Gao, H., Wei, Y., Mlynczak, M. G., and Russell III, J. M.: Strong longitudinal variations in the OH nightglow, Geophys. Res. Lett., 37, L21801, doi:10.1029/2010GL043972, 2010.

Xu, J., Gao, H., Smith, A. K., and Zhu, Y.: Using TIMED/SABER nightglow observations to investigate hydroxyl emission mechanisms in the mesopause region, J. Geophys. Res., 117, D02301, doi:10.1029/2011JD016342, 2012.

Figures

Figure 1. Observed at 43° N (black line) and modelled at 43.75° N (red line) annual variability of intensity and volume emission (a), temperature (b), atomic oxygen concentration (c), and height at the peak of the $OH^*_{v=6}$ layer.

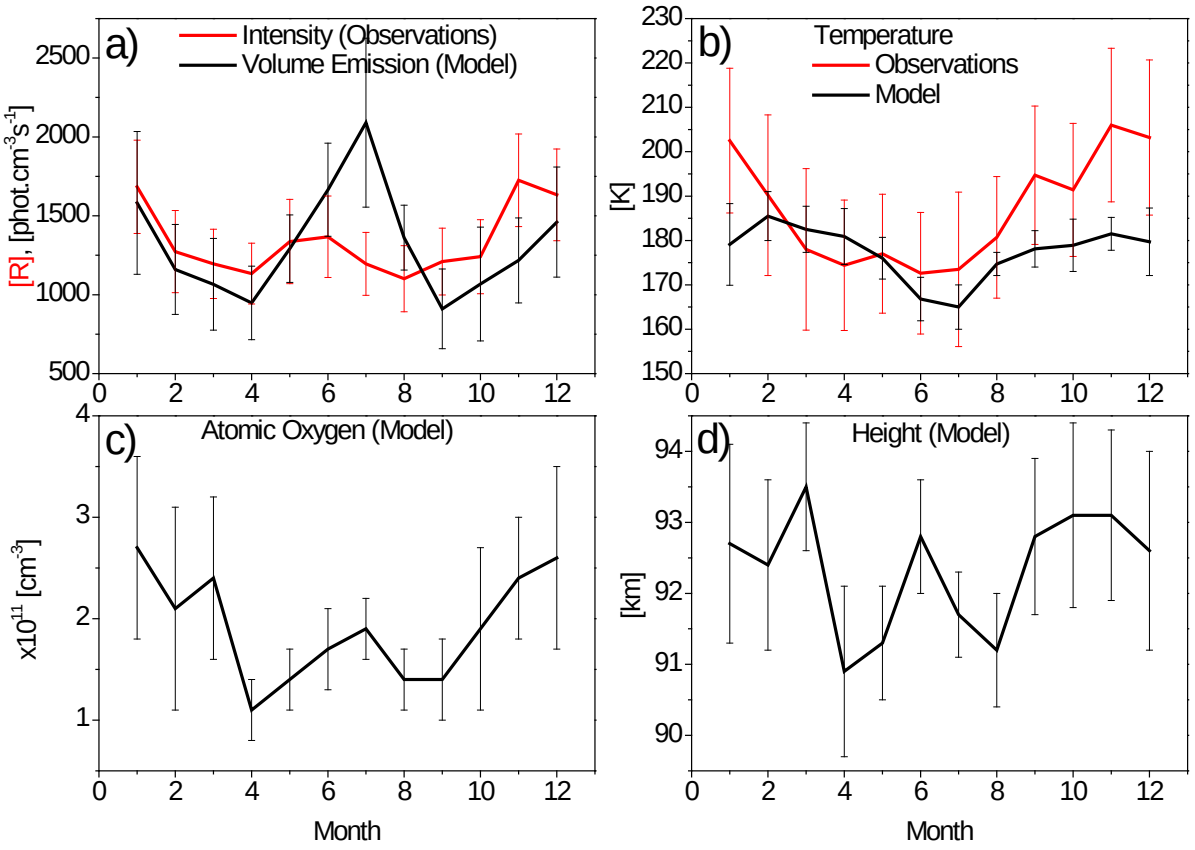

Figure 2. Nightly mean one-month sliding averaged volume emission (a), temperature (b), atomic oxygen at peak of $OH^*_{v=6}$ (c), and height of peak of $OH^*_{v=6}$.

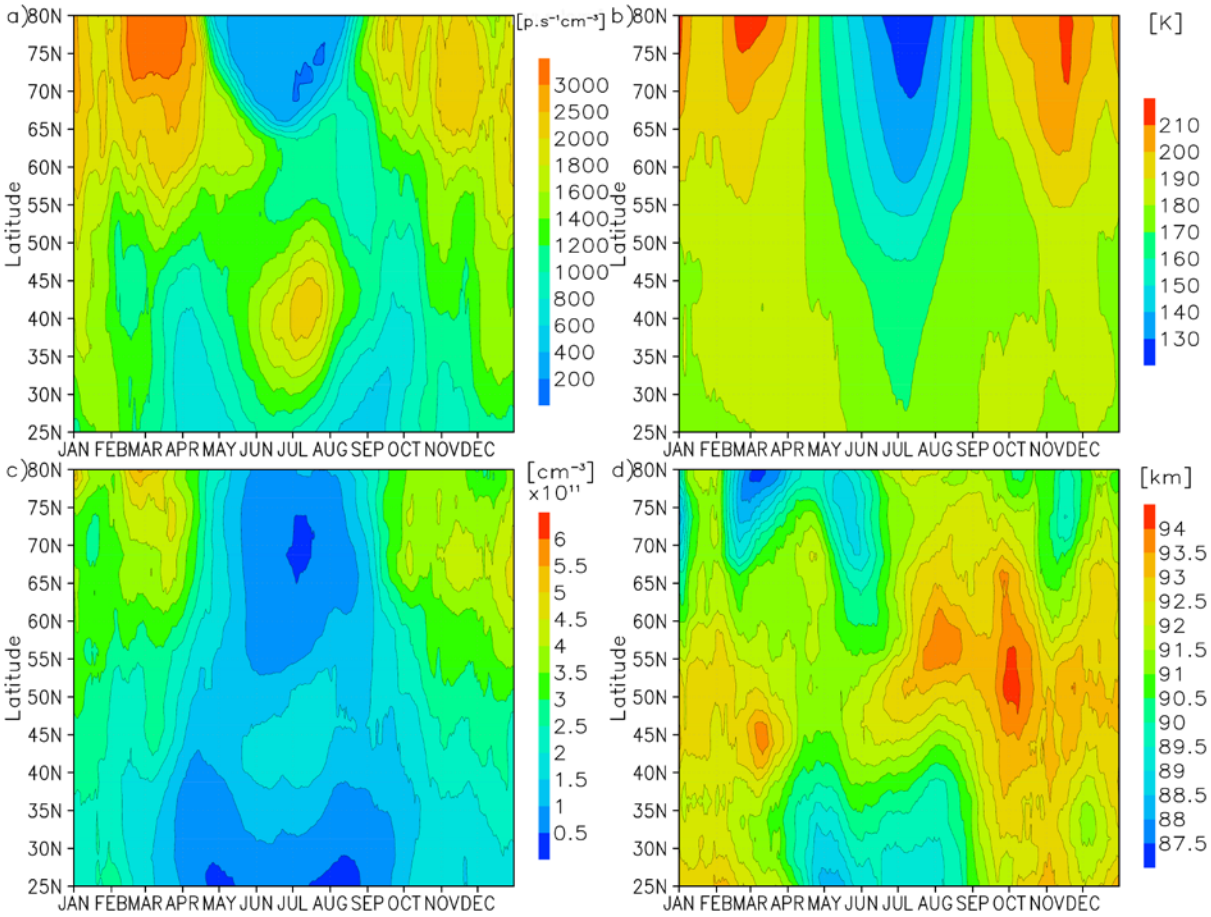

Figure 3. a) relative to annual averaged variations of volume emission due to atomic oxygen (black line), temperature (red line), and height (green line) at 43.75° N; b) relative variations of volume emission due to second momentum $\frac{[O]'M'}{\overline{[O]}\bar{M}}$ (blue line), $\frac{T'M'}{\bar{T}\bar{M}}$ (cyan line), and $\frac{[O]'T'}{\overline{[O]}\bar{T}}$ (magenta line) at 43.75° N.